Materials and Design 192 (2020) 108716

Contents lists available at ScienceDirect

Materials and Design

journal homepage: www.elsevier.com/locate/matdes

Design of a dual-phase hcp-bcc high entropy alloy strengthened by ω nanoprecipitates in the Sc-Ti-Zr-Hf-Re system

Lukasz Rogal [a,**], Yuji Ikeda [b,c,*], Minjie Lai [d], Fritz Körmann [b,e], Alicja Kalinowska [a], Blazej Grabowski [c]

[a] Institute of Metallurgy and Materials Science, Polish Academy of Sciences, 25, Reymonta Street, 30-059 Krakow, Poland
[b] Computational Materials Design, Max-Planck-Institut für Eisenforschung GmbH, 40237 Düsseldorf, Germany
[c] Institute of Materials Science, University of Stuttgart, Pfaffenwaldring 55, 70569 Stuttgart, Germany
[d] State Key Laboratory of Solidification Processing, Northwestern Polytechnical University, 710072 Xi'an, China
[e] Materials Science and Engineering, Delft University of Technology, 2628 CD Delft, the Netherlands

HIGHLIGHTS

- *Ab initio* calculations demonstrate the stabilization of the bcc and the ω phases when adding Re to the Sc-Ti-Zr-Hf system,
- Detailed experimental observations including TEM analysis confirm the stabilization and reveal ω nanoparticles,
- A mechanically superior dual-phase bcc +hcp microstructure strengthened by ω nanoparticles is designed

GRAPHICAL ABSTRACT

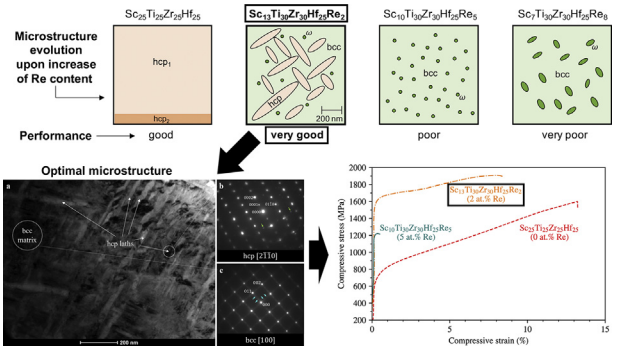

ARTICLE INFO

Article history:
Received 24 February 2020
Received in revised form 26 March 2020
Accepted 2 April 2020
Available online 4 April 2020

Keywords:
ω phase
High entropy alloys
ab initio simulations
Dual-phase HEA
TEM studies

ABSTRACT

High entropy alloys (HEAs) in the hexagonal close-packed (hcp) phase usually show poor mechanical properties. We demonstrate here, by use of *ab initio* simulations and detailed experimental investigations, that the mechanical properties can be improved by optimizing the microstructure. In particular we design a dual-phase HEA consisting of a body-centered cubic (bcc) matrix and hcp laths, with nanoprecipitates of the ω phase in the Sc-Ti-Zr-Hf-Re system, by controlling the Re content. This dedicated microstructure reveals, already in the as-cast state, high compressive strength and good ductility of 1910 MPa and 8%, respectively. Our study lifts the hcp-based HEAs onto a competitive, technological level.

1. Introduction

In the recent decade, significant efforts have been put forward in developing high entropy alloys (HEAs) [1–9]. The vast majority of HEAs crystalizes on a face-centered cubic (fcc) or body-centered cubic (bcc) lattice. More recently, hexagonal close-packed (hcp) HEAs have been found [10–15]. Youssef et al. [10] obtained for example an

* Corresponding author.
** Correspondence to: L. Rogal, Institute of Metallurgy and Materials Science, Polish Academy of Sciences, 25, Reymonta Street, 30-059 Krakow, Poland.
E-mail addresses: l.rogal@imim.pl (L. Rogal), yuji.ikeda@imw.uni-stuttgart.de (Y. Ikeda).

https://doi.org/10.1016/j.matdes.2020.108716

$Al_{20}Li_{20}Mg_{10}Sc_{20}Ti_{30}$ hcp HEA using heat-treated mechanically-alloyed powders. Hcp solid solutions were also reported for equiatomic CoFeReRu and CoReRuV [11]. Nearly single-phase hcp structures were found in cast YGdTbDyLu, GdTbDyTmLu [12] and HoDyYGdTb [13] alloys. Mo-Ru-Rh-Pd and Mo-Tc-Ru-Rh-Pd alloys show the hcp phase [16,17], which was investigated using *ab initio* calculations [18]. Despite these works, the hcp HEA field is still in its infancy, and it is therefore desirable to further enhance their microstructural and mechanical properties. An appealing path to improve the mechanical properties is by tuning the phase composition or by introducing strengthening precipitates. For example, it is known that a mixture of bcc and hcp phases leads to an optimal combination of strength and ductility for the conventional Ti-6Al-4 V wt% alloy [19].

In the present work the chemical composition of an hcp-based Sc-Ti-Zr-Hf-Re HEA is optimized by tuning the Re content in order to obtain a beneficial dual-phase microstructure of hcp and bcc with ω nanoprecipitates. The related equiatomic hcp ScTiZrHf HEA was studied in detail in Ref. [14]. ScTiZrHf exhibits a mixture of two hcp solid solutions, a relatively low yield strength, and similarities to Ti alloys (similar morphology [14] and ordering tendency when alloyed with Al [15]). For Ti, it is known that Re stabilizes the bcc structure and affects material properties [20]. In particular, Re considerably raises hardness, strength, recrystallization temperature and corrosion resistance (Ref. [21] and references therein). Ti-alloy properties can be also modified by the formation of the hexagonal ω phase [22,23]. In Refs. [24, 25] metastable β-titanium alloys with a variable Young's modulus were developed based on deformation-induced ω. Lai et al. [26] studied the effect of the ω phase on the deformation mechanism of a metastable Ti-Nb-based alloy revealing an enhanced yield strength. Experimental studies on ω phase formation in Re-containing Ti alloys are lacking so far. Only a single theoretical, *ab initio* based study was performed [20], showing the possibility of ω formation in the Ti—Re binary system.

The objective of the present work is to determine the impact of Re on the as-cast microstructure and mechanical properties of the Sc-Ti-Zr-Hf-Re system. For that purpose, we choose the following set of HEAs: $Sc_{13}Ti_{30}Zr_{30}Hf_{25}Re_2$, $Sc_{10}Ti_{30}Zr_{30}Hf_{25}Re_5$, and $Sc_7Ti_{30}Zr_{30}Hf_{25}Re_8$ (at.%); *i.e.*, alloys with an increasing Re concentration at the expense of Sc, which shows the strongest tendency for precipitation [14,15]. Another guiding principle for decreasing Sc concentration is an improvement of the economic factor. As a reference we compare our results to the previously investigated equiatomic $Sc_{25}Ti_{25}Zr_{25}Hf_{25}$ alloy. *Ab initio* calculations and detailed experimental investigations are conducted to investigate the phase stability and to elucidate the impact of Re on microstructure and mechanical properties.

2. Methodological details

2.1. Material preparation

The alloys were prepared of elements of 99.99 wt% purity in an arc melting furnace with a water-cooled copper plate under a protective Ar atmosphere. High purity titanium was applied as a getter. To ensure sufficient homogenization, the alloys were re-melted 5 times. The samples of each batch were prepared with a target weight of 3.5 g and cylindrical shape of 10 mm in height and 10 mm in diameter. Overall alloy compositions were determined using large area (1600 μm × 1600 μm) Scanning Electron Microscopy/Energy Dispersive X-Ray Spectroscopy (Table I). Since the alloy with 8 at.% Re showed high brittleness, this alloy is omitted from most of our analyses below. All the newly designed alloys solidified under conventional arc-melting and water-cooled copper-mold cooling conditions.

2.2. Microstructural and mechanical properties analysis

All alloys were characterized in the as-cast state. Platelets with a thickness of 4 mm were sectioned for the structural characterization from the bottom of the cast. The X-ray measurements of the phase composition were performed using a D2 Phaser-Bruker diffractometer and Co-Kα filtered radiation. The microstructure was examined using a scanning electron microscope FEI SEM XL30 (FEI Company, Hillsboro, OR) equipped with an energy-dispersive X-ray spectrometer EDAX GEMINI 4000. The microstructure and selected area electron diffraction pattern (SAEDP) studies were performed using a Tecnai G2 F20 transmission electron microscope (TEM). The microchemical analysis was conducted using the TEM equipment in both transmission and in scanning transmission (STEM) modes coupled with Integrated Energy-Dispersive X-ray spectroscopy (EDS). The samples for TEM were thinned using Struers Tenupol-5 jet polisher (Struers, Inc., Cleveland, OH) in an electrolyte consisting of 20 vol% $HClO_4$ and 80 vol% CH_3OH at subzero temperatures. The Vickers hardness was measured under a load of 5 kg using a Zwick/ZHU 250 tester. The compression strength tests were performed with an Instron 6025 testing machine at room temperature.

Table I
Overall compositions of the investigated alloys measured using large area Scanning Electron Microscopy/Energy Dispersive X-Ray Spectroscopy. Note that samples of local compositions of different nanostructures are summarized separately in Table A1.

	Content (at.%)				
	Sc	Ti	Zr	Hf	Re
$Sc_{13}Ti_{30}Zr_{30}Hf_{25}Re_2$	13.1	31.2	28.9	24.7	2.1
$Sc_{10}Ti_{30}Zr_{30}Hf_{25}Re_5$	9.7	30.8	29.4	25.2	4.9
$Sc_7Ti_{30}Zr_{30}Hf_{25}Re_8$	6.8	28.6	28.6	27.3	8.7

2.3. Ab initio calculations

For the *ab initio* calculations primitive cells including one, two, and three atoms were considered as the unit cells of the bcc, hcp and ω phases, respectively. For the hcp phase an ideal c/a ratio of $\sqrt{8/3} \approx 1.633$ has been chosen. To keep coherency between the ω and bcc phase, the c/a ratio for the ω phase has been fixed to $\sqrt{3/8} \approx 0.612$. The electronic structure calculations were performed employing the exact-muffin-tin-orbital (EMTO) method [27–31] in combination with the full-charge-density (FCD) method [32,33] within the framework of density functional theory (DFT). Chemical disorder was modeled based on the coherent-potential approximation (CPA) [34–36]. The charges and the energies were calculated within the generalized-gradient approximation (GGA) of the Perdew-Burke-Ernzerhof (PBE) form [37]. The Brillouin zones were sampled by 24 × 24 × 24, 22 × 22 × 13, and 14 × 14 × 23 k-point meshes for the bcc, hcp, and ω unit cells, respectively. To obtain the energy-volume curves, total energies at 13 volumes from 18 $Å^3$/atom to 24 $Å^3$/atom were computed for each composition and for each phase. Atoms were fixed to their ideal lattice sites. The equilibrium properties were determined by fitting the energy-volume data to the Vinet equation of state (EOS) [38,39].

3. Results and discussion

3.1. Ab initio calculations of phase stabilities

In order to quantitatively assess the bcc-hcp-ω phase stabilities for the selected compositions, we resort to *ab initio* calculations. Fig. 1 shows the computed energy-volume curves for the investigated alloys. For the Re-free $Sc_{25}Ti_{25}Zr_{25}Hf_{25}$ alloy, the hcp phase is found to be the most stable one at 0 K. This is in contrast to the three Re-containing alloys for which the ω phase is found to be energetically more favorable. It is also found that adding Re energetically stabilizes the bcc and the ω phases compared to hcp phase. For the $Sc_7Ti_{30}Zr_{30}Hf_{25}Re_8$ composition all three phases have very similar energies.

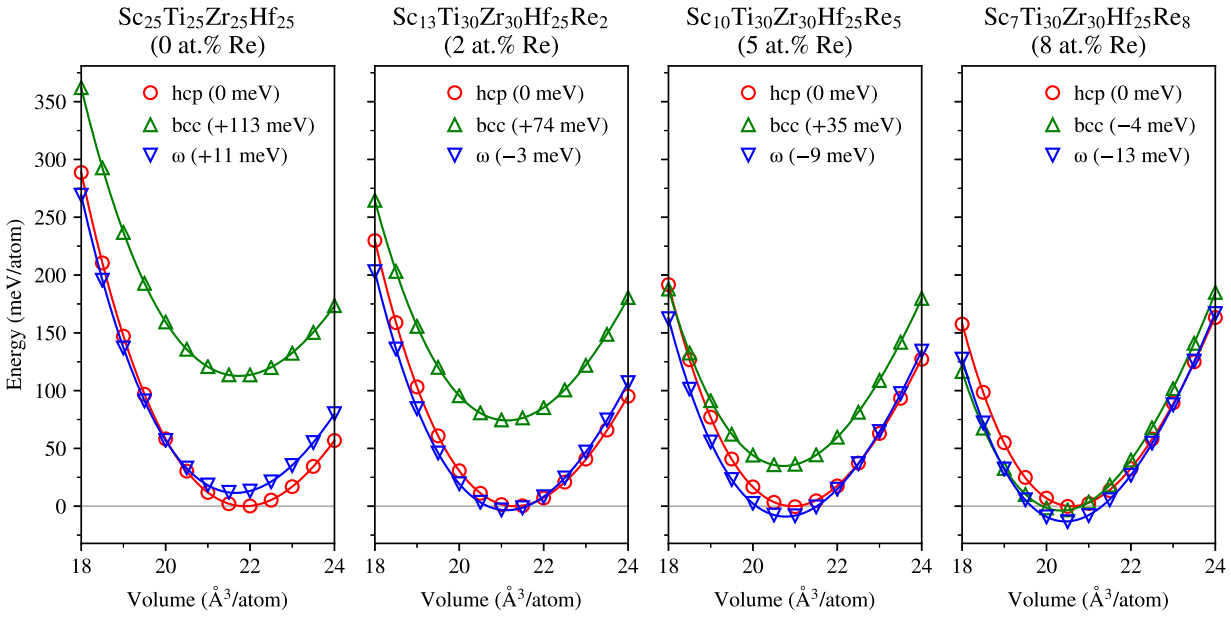

Fig. 1. Energy-volume curves at 0 K for the investigated alloys obtained by the *ab initio* calculations. The energy of the hcp phase at the equilibrium volume is set as the reference and indicated by a horizontal gray line for each composition. Energy differences at the equilibrium volumes are indicated in the legend.

3.2. Microstructure analysis

All as-cast alloys exhibit a morphology typical for arc melted samples, in which crystallization starts from the bottom copper plate [40]. Some segregation of elements is observed as typically found for as-cast structures. Details are given in the Appendix.

The X-ray diffraction (XRD) analysis shown in Fig. 2 reveals a change of the microstructure with increasing Re content. For the equiatomic $Sc_{25}Ti_{25}Zr_{25}Hf_{25}$ alloy without Re (0 at.% Re) only hcp reflections are visible. The 2 at.% Re alloy ($Sc_{13}Ti_{30}Zr_{30}Hf_{25}Re_2$) shows an hcp-bcc dual-phase structure. For the Re content of 5 at.% ($Sc_{10}Ti_{30}Zr_{30}Hf_{25}Re_5$), the XRD pattern shows a strong signature of bcc with additional weak

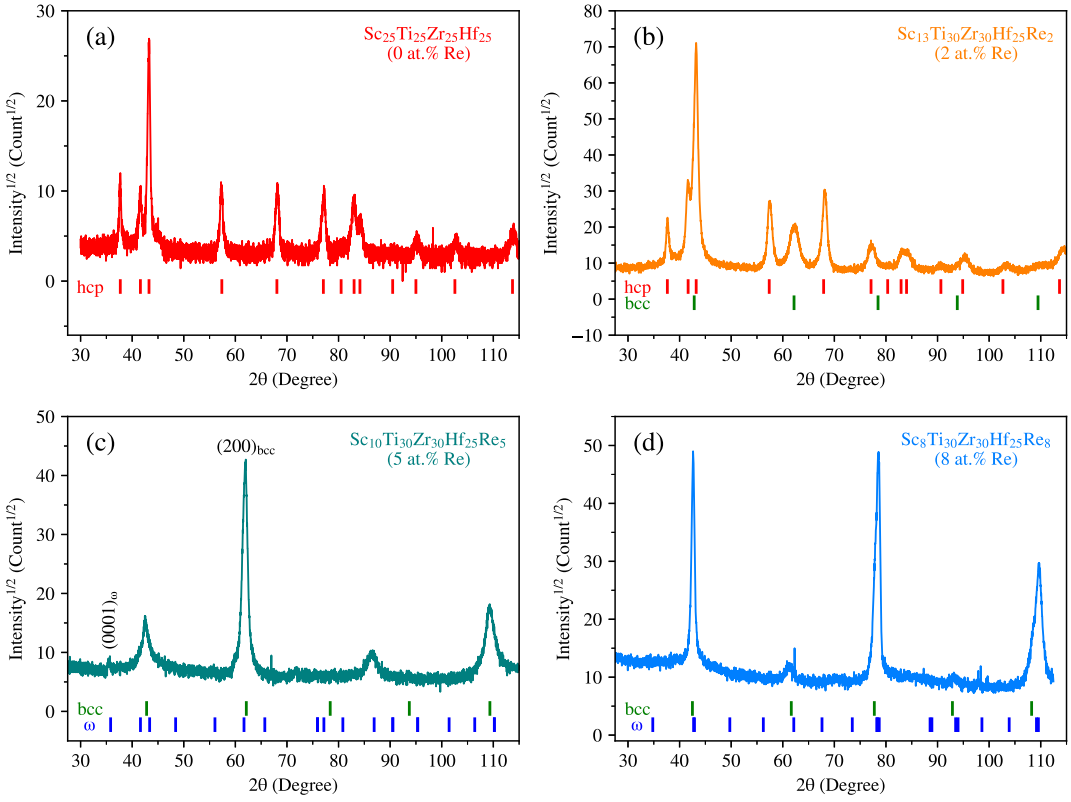

Fig. 2. XRD patterns of (a) equiatomic $Sc_{25}Ti_{25}Zr_{25}Hf_{25}$ without Re (0 at.% Re), (b) $Sc_{13}Ti_{30}Zr_{30}Hf_{25}Re_2$ (2 at.% Re), (c) $Sc_{10}Ti_{30}Zr_{30}Hf_{25}Re_5$ (5 at.% Re), and (d) $Sc_7Ti_{30}Zr_{30}Hf_{25}Re_8$ (8 at.% Re). Ideal peak positions of the phases identified by a Rietveld-analysis are shown at the bottom of the XRD spectra.

peaks, *e.g.*, at the 2θ of 36 and 77 degrees, which can be assigned to the ω phase. Also for the 8 at.% Re alloy ($Sc_7Ti_{30}Zr_{30}Hf_{25}Re_8$) we observe both bcc and ω reflections in the XRD pattern. The observed stabilization of the bcc and ω phases with respect to the hcp phase when increasing the Re content is consistent with our *ab initio* results of the previous section.

Note, however, that while the calculated chemical trend is in good agreement with the experiments, there appears to be a discrepancy in the prediction of the phase stabilities. For example, the 5% Re alloy shows a strong XRD pattern of bcc whereas *ab initio* predicts the bcc phase to be about 35 meV/atom above hcp in energy. This discrepancy is very likely caused by missing lattice distortions [41–44], which cannot be in general captured by CPA calculations, and by finite-temperature excitations [41,43,45–49]. An explicit calculation of these effects is computationally very demanding and beyond the scope of our study. However, we can give a reasonable estimate of the impact of both effects based on previous works. It was reported [42] that the energy gain due to relaxation of atomic positions is larger for bcc HEAs, particularly those with large amounts of group-4 elements (Ti, Zr, Hf) (relaxation energies: 40–80 meV/atom), than for the HEAs with close-packed structures (relaxation energies: 5–10 meV/atom). Considering these relaxation energies, the bcc phase can be expected to be energetically stabilized furthermore by roughly 50 meV/atom, *i.e.*, the bcc energy-volume curves in Fig. 1 (green curves) would be lowered by such an amount. Finite temperature effects, in particular vibrations, can be also expected to stabilize the bcc phase due to a strong anharmonic contribution [50]. Overall we can thus anticipate that considering these effects would bring the *ab initio* results in better agreement with the experimental observations.

The TEM bright-field (BF) image (Fig. 3) reveals that the 2 at.% Re hcp-bcc dual-phase alloy exhibits a microstructure with very fine hcp laths, suggesting a diffusionless nucleation process. The hcp laths have sizes up to 300 nm in length and 20–40 nm in thickness and are oriented at $[2\bar{1}\bar{1}0]$ with respect to the bcc matrix with [100] zone axis. Similar laths of hcp or orthorhombic martensitic phases were reported also for Ti-Nb-based alloys [51,52]. The SAEDP from the laths (Fig. 3(b)) essentially shows the pattern of an hcp phase, but we see *e.g.* the (0001) reflection, which is forbidden in the ideal case. The occurrence of the (0001) reflection indicates long-range ordering in the hcp phase [53]. In the SAEDP from the bcc matrix (Fig. 3(c)), weak reflections (indicated by the blue arrows) are found at the 1/3 and 2/3 positions along the {110} systematic rows. These weak reflections indicate long-range ordering in the bcc matrix as well. Similar spots were found in the Ti-5Al-5Mo-5V-3Cr wt% (Ti-5553) alloy [54]. Note, however, that the pattern of the weak spots shown in Fig. 3(c) is different from that for the B2 phase, which was previously found or predicted for other bcc HEAs in experiments [55] or by *ab initio* methods [41,44,49,56–64], respectively. The weak spots in Fig. 3(c) are also not the double diffraction of the bcc phase, which was found in the quenched Ti-4Al-4Fe-0.25Si-0.1O (wt%) alloy [65]. In Fig. 3(c) we further observe weak diffuse scattering along the {110} systematic rows. This may originate from incipient short-range ordering or local lattice distortions in the bcc matrix. Similar diffuse scattering was found also in the interdendritic region of a AlCoCrFeNi HEA [66].

Fig. 4 shows TEM results of the 2 at.% Re alloy from another crystallographic orientation ($[110]_{bcc}$ zone axis) of the bcc matrix and reveals the occurrence of nanoprecipitates. The dark-field (DF) image shown in Fig. 4(c), obtained with the reflection marked with a circle in the SAEDP in Fig. 4(b), indicates that the nanoparticles have spherical shape with an average diameter of 25 nm. The $[110]_{bcc}$ SAEDP in Fig. 4 (b) demonstrates that the nanoparticles are coherent with the bcc matrix, and from the comparison with previous literature [67–69] the nanoparticles can be assigned to the ω phase with two orientation variants. This ω phase in the 2 at.% Re alloy could not be detected by the above-discussed XRD-analysis because of the small size of the nanoparticles. The orientation relationship derived from the SAEDPs of $[110]_{bcc}$ (Fig. 4(b)) and other zone axes are $(110)_{bcc}//(2\bar{1}\bar{1}0)_{\omega 1}$, $[1\bar{1}2]_{bcc}//[01\bar{1}0]_{\omega 1}$, and $[1\bar{1}\bar{1}]_{bcc}//[0001]_{\omega 1}$, where ω1 indicates one of the orientation variants of the ω phase. Note that the SAEDP in Fig. 4(b) also shows satellite spots (indicated by the blue arrows) near the bcc reflections; previous literature suggests that they may originate from the hcp (α) phase [70].

For the 5 at.% Re $Sc_{10}Ti_{30}Zr_{30}Hf_{25}Re_5$ alloy our TEM results reveal a stronger signature of the ω nanoprecipitates in the bcc matrix (see Appendix). This is consistent with the XRD results, which already indicated the appearance of the ω phase in this alloy. No TEM

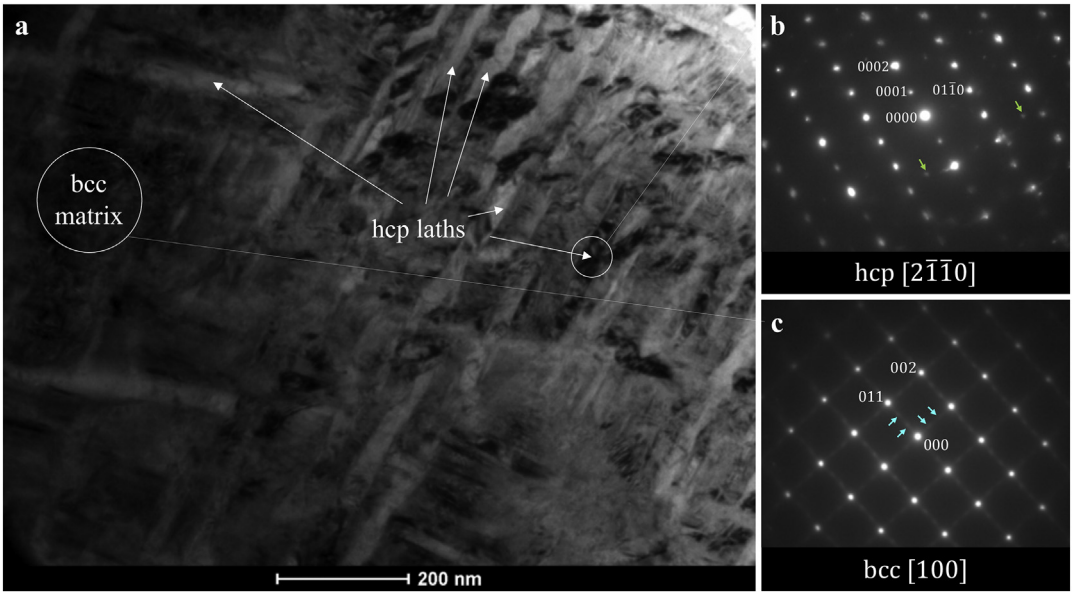

Fig. 3. (a) TEM bright-field image of the $Sc_{13}Ti_{30}Zr_{30}Hf_{25}Re_2$ HEA for the area including hcp laths and the bcc matrix. (b) SAEDP from the hcp laths. Green arrows indicate reflections from the surrounding bcc matrix. (c) SAEDP from the bcc matrix. Blue arrows indicate reflections which may originate from a long-range ordering in the bcc matrix.

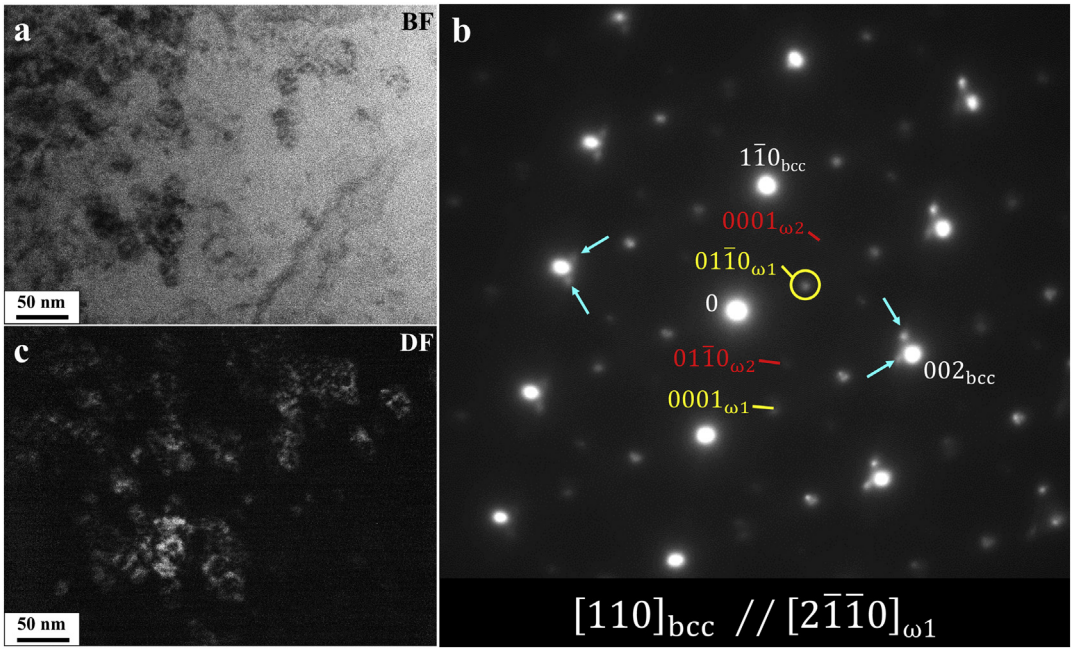

Fig. 4. TEM observations of the bcc matrix in the $Sc_{13}Ti_{30}Zr_{30}Hf_{25}Re_2$ HEA. (a) BF image of plates. (b) SAEDP. (c) DF image from the $(01\bar{1}0)_{\omega 1}$ reflection, showing bright contrasted regions of ω-phase precipitations.

analysis was performed for the brittle 8 at.% Re alloy ($Sc_7Ti_{30}Zr_{30}Hf_{25}Re_8$). However, based on the XRD results revealing ω reflections and the brittle behavior, we can speculate that the ω precipitates in the 8 at.% Re alloy are larger than the ones in the 5 at.% Re alloy and that they are responsible for the high brittleness. A similar embrittlement behavior due the ω phase was reported also for Ti-based alloys [22]. The increase of the ω-phase amount due to the addition of Re is, as already mentioned, consistent with the stabilization of the ω phase predicted by the *ab initio* calculations in this paper (Fig. 1).

Two mechanisms of ω phase formation have been distinguished in the literature: (i) athermal ω, formed by quenching from the β-phase (bcc) field; and (ii) isothermal ω, formed during low-temperature ageing of the β phase [71,72]. In the present study the ω phase forms as a result of rapid cooling during the crystallization of the ingot, and it is likely the athermal mechanism driving the transformation. The formation of ellipsoidally shaped metastable ω particles was also reported in low-misfit Ti—Mo alloys upon water quenching past solution treatment [73,74]. The formation of the ω phase in β-titanium alloys is in general associated with local rejection of β stabilizing elements resulting in a local compositional instability [23,72–75].

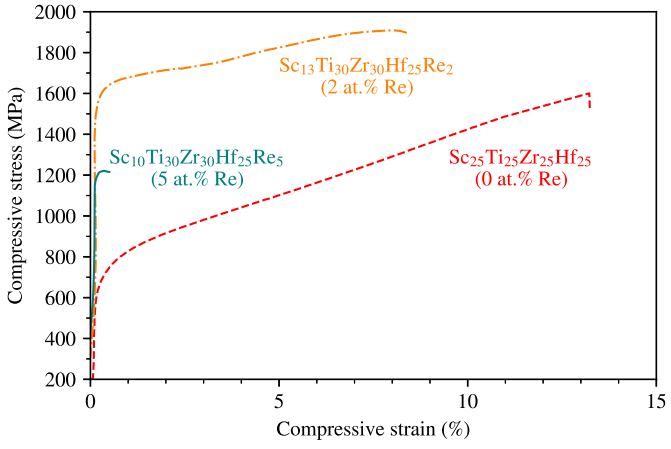

Fig. 5. Compressive stress-strain curves of the $Sc_{25}Ti_{25}Zr_{25}Hf_{25}$ (black dashed), $Sc_{13}Ti_{30}Zr_{30}Hf_{25}Re_2$ (red dash-dotted), and $Sc_{10}Ti_{30}Zr_{30}Hf_{25}Re_5$ (blue solid) alloys.

3.3. Deformation behavior

Results of the compression tests conducted on the as-cast samples are presented in Fig. 5 and Table II. The stress-strain plots clearly show a different material response depending on the chemical composition. For the equiatomic $Sc_{25}Ti_{25}Zr_{25}Hf_{25}$ alloy without Re (from Ref. [14]), an ultimate compressive strength of 1615 MPa is accompanied by a total strain of 13%, while the yield strength and hardness are only 698 MPa and 261 HV, respectively. The $Sc_{13}Ti_{30}Zr_{30}Hf_{25}Re_2$ HEA exhibits a significant increase of the yield strength up to 1550 MPa and an ultimate compressive strength and ductility of 1910 MPa and 8%, respectively. The hardness of the sample is 516 HV. For the alloy with 5% Re, the yield strength is 1100 MPa, and the compressive strength 1200 MPa at a low ductility of below 1%. The 8 at.% Re alloy is fully brittle and has the hardness of 473 HV.

As the mechanical tests reveal, the $Sc_{13}Ti_{30}Zr_{30}Hf_{25}Re_2$ HEA shows good mechanical properties. This good performance is due to the beneficial mixture of the hcp and bcc solid solution, the latter supported with

Table II
Measured mechanical properties of the investigated alloys. UCS and YS stand for ultimate compressive strength and yield strength, respectively.

	UCS (MPa)	YS (MPa)	Strain (%)	Hardness (HV)
$Sc_{25}Ti_{25}Zr_{25}Hf_{25}$	1615	698	13	261 ± 12
$Sc_{13}Ti_{30}Zr_{30}Hf_{25}Re_2$	1910	1550	8	516 ± 9
$Sc_{10}Ti_{30}Zr_{30}Hf_{25}Re_5$	1200	1120	0.5	436 ± 14

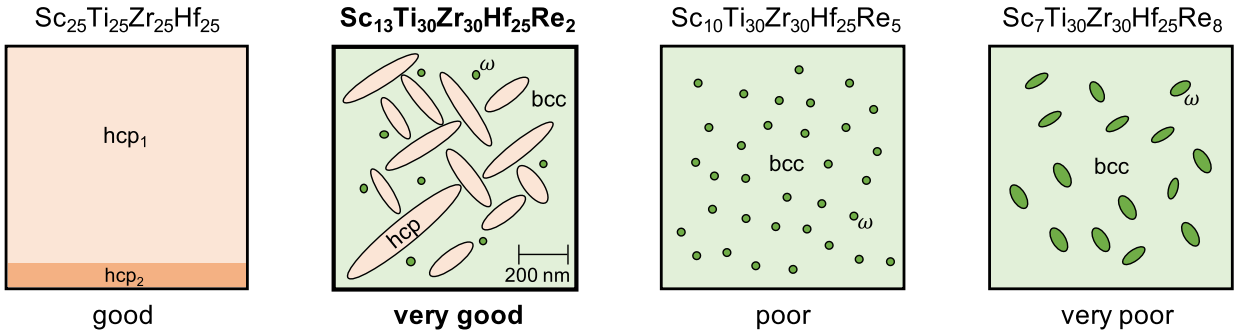

Fig. 6. Sketch of the microstructure for the series of investigated alloys with increasing Re-content from left to right. The 2 at.% Re-containing dual-phase HEA with nano-ω precipitates shows very good mechanical properties. Adding more Re, the hcp phase is destabilized and the ω phase particles are enlarged on the expense of the mechanical performance (as indicated at the bottom).

fine nanoprecipitates of the ω phase. The hcp phase is likely responsible for the good ductility of $Sc_{13}Ti_{30}Zr_{30}Hf_{25}Re_2$, as can be deduced from the good ductile behavior of the pure hcp based $Sc_{25}Ti_{25}Zr_{25}Hf_{25}$ alloy [14]. The ω nanoprecipitates are responsible for the increase in yield strength as confirmed in several previous works [23,26]. Increasing the Re content to 5 at.% Re leads to the formation of a single bcc solid solution structure with a high density of ω nanoparticles, which are homogenously distributed in the grains. It is known that a too high density of the ω phase can cause embrittlement in metastable β Ti alloys, due to a rapid increase of local elastic strains around the interface between the ω phase and β matrix [23]. It seems that the modulus of elasticity mismatch between the ω and the bcc phases probably plays the key role in loss of ductility in the bcc solid solution.

4. Conclusions

The effect of Re content on the microstructure and mechanical properties of the Sc-Ti-Zr-Hf-Re system has been studied by *ab initio* calculations and experiments. The alloys have been obtained by arc-melting of high purity elemental precursors and have been investigated in the as cast state. The best mechanical performance has been revealed for the 2 at.% Re-containing alloy which exhibits an hcp-bcc dual-phase microstructure with nanoprecipitates of the ω phase (*cf.* sketch in Fig. 6). Its compressive yield strength is 1550 MPa, the ultimate compressive strength 1910 MPa, and the total strain 8%. For comparison, the compressive yield strengths of technologically important Ti-based alloys are, *e.g.*, 970 MPa for the Ti-6Al-4 V wt% alloy (an α + β alloy) [76], 1100 MPa for the Ti-8Al-1Mo-1 V wt% alloy (a near-α alloy) [77], and 1200 MPa for the Ti-11.5Mo-6Zr-4.5Sn wt% alloy (a metastable β alloy) [76].

Our *ab initio* calculations demonstrate the energetic stabilization of the bcc and the ω phases when adding Re to the Sc-Ti-Zr-Hf system. The stabilization of both phases over hcp is confirmed by experiments. Increasing the Re concentration to 5 at.% or higher renders the bcc phase too stable and the beneficial hcp lath structure disappears deteriorating the mechanical properties. For 8 at.% Re the stability of the ω phase further increases, which enhances the growth of larger particles causing very high brittleness.

Our results demonstrate the capability to employ thermodynamic calculations from *ab initio* theory, to predict the stabilization of bcc and ω over the hcp phase, and with this to tune the microstructure in the Sc-Ti-Zr-Hf-Re system. The *ab initio* derived bcc-hcp-ω energetic differences could therefore in general be useful as materials property descriptors for screening and designing dual-phase hcp-bcc high entropy alloys strengthened by nanoprecipitates.

CRediT authorship contribution statement

Lukasz Rogal: Investigation, Formal analysis, Writing - original draft, Conceptualization. **Yuji Ikeda:** Investigation, Writing - original draft. **Minjie Lai:** Investigation .**Fritz Körmann:** Investigation. **Alicja Kalinowska:** Investigation. **Blazej Grabowski:** Investigation, Writing - original draft.

Declaration of competing interest

The authors declare that they have no known competing financial interests or personal relationships that could have appeared to influence the work reported in this paper.

Acknowledgements

We thank Nikolay Zotov for fruitful discussions. The research was supported by the Polish science financial resources The National Science Centre, Poland, project title: “Development of new high entropy alloys with dominant content of hexagonal solid solutions” project number: UMO-2014/15/D/ST8/02638. Support from the Deutsche Forschungsgemeinschaft (SPP 2006), NWO/STW (VIDI grant 15707), and the European Research Council (ERC) under the EU's Horizon 2020 Research and Innovation Programme (Grant no. 639211) are also gratefully acknowledged.

Appendix A

Here we provide additional experimental microstructural information. Light images of the 2 and 5 at.% Re alloys taken perpendicular to the direction of the crystallization of the drops are shown in Fig. A1(a) and (b). They reveal elongated grains with widths of 100–600 μm and lengths of 200–2000 μm with a fine dendritic microstructure inside. SEM images are shown in Fig. A1(c) and (d). They reveal columnar dendrites with some Zr and Ti segregation visible as contrast changes (*cf.* EDS analysis in Table A1). The STEM image of the $Sc_{13}Ti_{30}Zr_{30}Hf_{25}Re_2$ HEA in Fig. A2 (a) confirms the lath-like microstructure. The EDS mappings of the area marked with a rectangular frame in Fig. A3(a) indicate that the laths are enriched in Sc and Hf (Figs. A2(b, c)), while the area between the laths is enriched in Ti and Re (Fig. A2(e, f)). Zr appears homogeneously distributed. The STEM/EDS images of the $Sc_{10}Ti_{30}Zr_{30}Hf_{25}Re_5$ HEA (Fig. A3) show a homogenous distribution for all the five elements with no indication of laths. The TEM image in Fig. A4 confirms the presence of the ω phase for the $Sc_{10}Ti_{30}Zr_{30}Hf_{25}Re_5$ HEA.

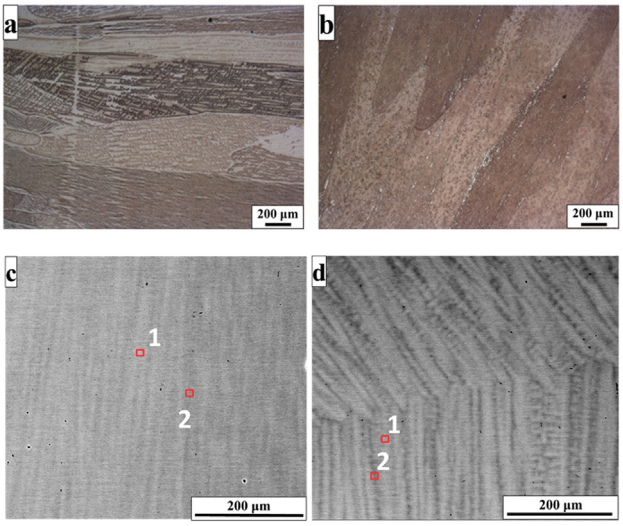

Fig. A1. Light images of (a) $Sc_{13}Ti_{30}Zr_{30}Hf_{25}Re_2$ and (b) $Sc_{10}Ti_{30}Zr_{30}Hf_{25}Re_5$ and SEM images of (c) $Sc_{13}Ti_{30}Zr_{30}Hf_{25}Re_2$ and (d) $Sc_{10}Ti_{30}Zr_{30}Hf_{25}Re_5$ with marked points of EDS analysis (Table A1).

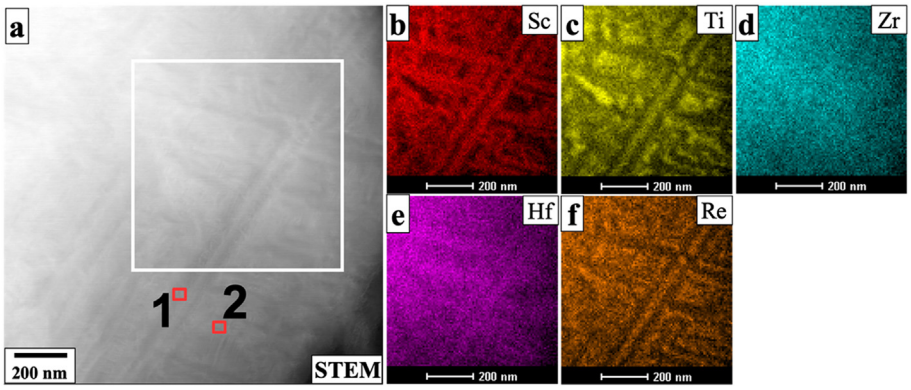

Fig. A2. (a) STEM image and (b–f) EDS mappings for the $Sc_{13}Ti_{30}Zr_{30}Hf_{25}Re_2$ HEA. The white frame in (a) indicates the area for the EDS mapping, and the red markers indicate the points of EDS analysis (Table A1).

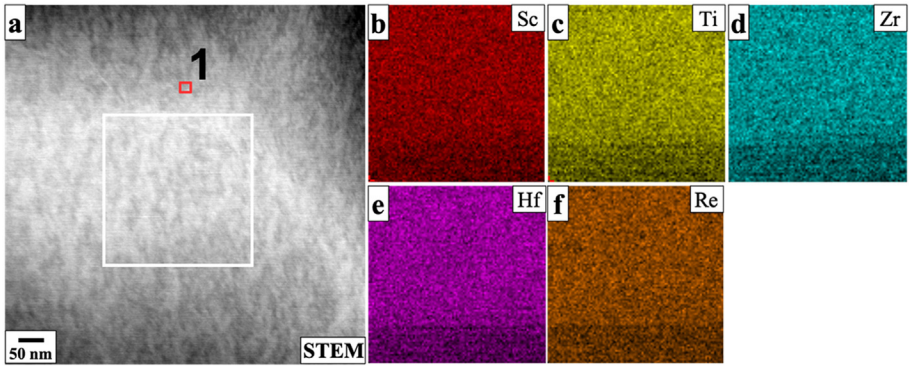

Fig. A3. (a) STEM image and (b–f) EDS mappings for the $Sc_{10}Ti_{30}Zr_{30}Hf_{25}Re_5$ HEA. The white frame in (a) indicates the area for the EDS mapping, and the red markers indicate the points of EDS analysis (Table A1).

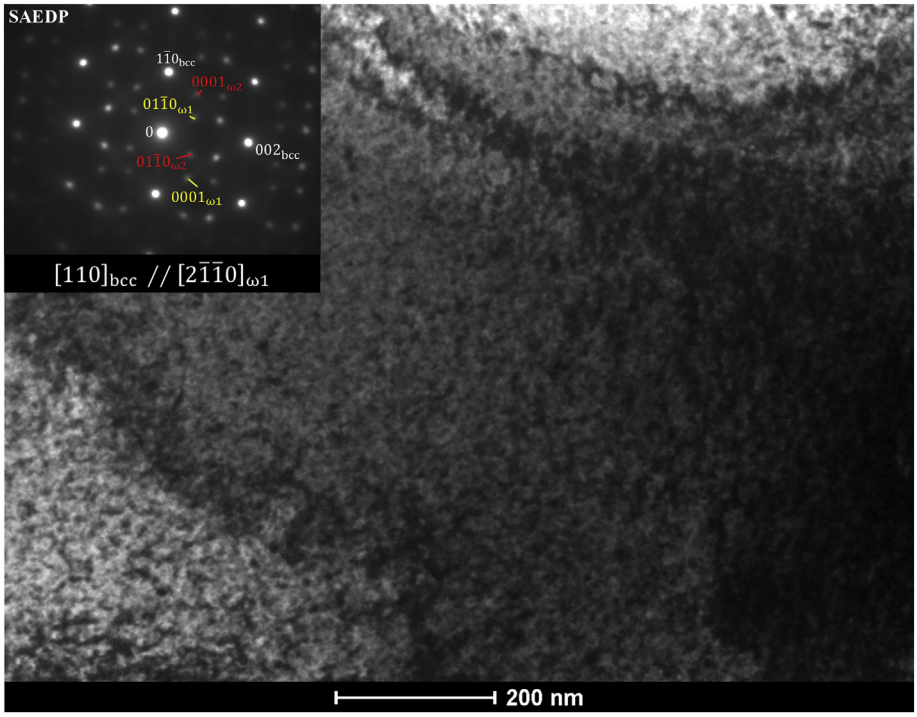

Fig. A4. TEM bright-field image of the $Sc_{10}Ti_{30}Zr_{30}Hf_{25}Re_5$ HEA along with SAEDP from the central part of micrograph.

Table A1
Results of EDS analysis in areas listed in Figs. A1 to A3.

Alloy type	Figure	Point of analysis	Phase	Volume (%)	Content (at.%)				
					Sc	Ti	Zr	Hf	Re
2 at.% Re	Fig. A1c SEM	1 – dendrite	hcp/bcc	57.2	12.7	29.8	28.5	26.4	2.5
		2 – interdendritic	hcp/bcc	42.8	10.9	25.6	34.7	26.3	2.4
	Fig. A2a TEM	1 – lath	hcp	52.3	11.3	26.6	32.9	28.5	0.6
		2 – matrix	bcc	46.7	7.3	26.4	36.9	26.9	2.3
5 at.% Re	Fig. A1d SEM	1 – dendrite	bcc	52.1	10.3	32.2	26.2	25.1	5.2
		2 – interdendritic	bcc	47.9	8.7	28.8	35.1	22.9	4.5
	Fig. A3a TEM	1 – matrix	bcc	100	9.4	25.5	31.4	29.1	4.5

References

[1] J.-W. Yeh, S.-K. Chen, S.-J. Lin, J.-Y. Gan, T.-S. Chin, T.-T. Shun, C.-H. Tsau, S.-Y. Chang, Nanostructured high-entropy alloys with multiple principal elements: novel alloy design concepts and outcomes, Adv. Eng. Mater. 6 (2004) 299–303https://doi.org/10.1002/adem.200300567.

[2] B. Cantor, I.T.H. Chang, P. Knight, A.J.B. Vincent, Microstructural development in equiatomic multicomponent alloys, Mater. Sci. Eng. A 375 (2004) 213–218, https://doi.org/10.1016/j.msea.2003.10.257.

[3] B.S. Murty, J.-W. Yeh, S. Ranganathan, High-entropy alloys, Butterworth-Heinemann, 2014.

[4] Y. Zhang, T.T. Zuo, Z. Tang, M.C. Gao, K.A. Dahmen, P.K. Liaw, Z.P. Lu, Microstructures and properties of high-entropy alloys, Prog. Mater. Sci. 61 (2014) 1–93, https://doi.org/10.1016/j.pmatsci.2013.10.001.

[5] M.C. Gao, J.-W. Yeh, P.K. Liaw, Y. Zhang, High-entropy Alloys: Fundamentals and Applications, Springer International Publishing, Cham, 2016.

[6] Y. Lu, Y. Dong, S. Guo, L. Jiang, H. Kang, T. Wang, B. Wen, Z. Wang, J. Jie, Z. Cao, H. Ruan, T. Li, A promising new class of high-temperature alloys: eutectic high-entropy alloys, Sci. Rep. 4 (2014) 6200, https://doi.org/10.1038/srep06200.

[7] F. He, Z. Wang, P. Cheng, Q. Wang, J. Li, Y. Dang, J. Wang, C.T. Liu, Designing eutectic high entropy alloys of CoCrFeNiNb$_x$, J. Alloys Compd. 656 (2016) 284–289, https://doi.org/10.1016/j.jallcom.2015.09.153.

[8] Ł. Rogal, J. Morgiel, Z. Świątek, F. Czerwiński, Microstructure and mechanical properties of the new $Nb_{25}Sc_{25}Ti_{25}Zr_{25}$ eutectic high entropy alloy, Mater. Sci. Eng. A 651 (2016) 590–597, https://doi.org/10.1016/j.msea.2015.10.071.

[9] L.J. Santodonato, Y. Zhang, M. Feygenson, C.M. Parish, M.C. Gao, R.J.K. Weber, J.C. Neuefeind, Z. Tang, P.K. Liaw, Deviation from high-entropy configurations in the atomic distributions of a multi-principal-element alloy, Nat. Commun. 6 (2015) 5964, https://doi.org/10.1038/ncomms6964.

[10] K.M. Youssef, A.J. Zaddach, C. Niu, D.L. Irving, C.C. Koch, A novel low-density, high-hardness, high-entropy alloy with close-packed single-phase nanocrystalline structures, Mater. Res. Lett. 3 (2014) 95–99, https://doi.org/10.1080/21663831.2014.985855.

[11] M.C. Gao, B. Zhang, S.M. Guo, J.W. Qiao, J.A. Hawk, High-entropy alloys in hexagonal close-packed structure, Metall. Mater. Trans. A 47 (2015) 3322–3332, https://doi.org/10.1007/s11661-015-3091-1.

[12] A. Takeuchi, K. Amiya, T. Wada, K. Yubuta, W. Zhang, High-entropy alloys with a hexagonal close-packed structure designed by Equi-atomic alloy strategy and binary phase diagrams, JOM 66 (2014) 1984–1992, https://doi.org/10.1007/s11837-014-1085-x.

[13] P.F. Yu, L.J. Zhang, J.L. Ning, M.Z. Ma, X.Y. Zhang, Y.C. Li, P.K. Liaw, G. Li, R.P. Liu, Pressure-induced phase transitions in HoDyYGdTb high-entropy alloy, Mater. Lett. 196 (2017) 137–140, https://doi.org/10.1016/j.matlet.2017.02.136.

[14] Ł. Rogal, F. Czerwinski, P.T. Jochym, L. Litynska-Dobrzynska, Microstructure and mechanical properties of the novel $Hf_{25}Sc_{25}Ti_{25}Zr_{25}$ equiatomic alloy with hexagonal solid solutions, Mater. Des. 92 (2016) 8–17, https://doi.org/10.1016/j.matdes.2015.11.104.

[15] L. Rogal, P. Bobrowski, F. Körmann, S. Divinski, F. Stein, B. Grabowski, Computationally-driven engineering of sublattice ordering in a hexagonal AlHfScTiZr high entropy alloy, Sci. Rep. 7 (2017) 2209, https://doi.org/10.1038/s41598-017-02385-w.

[16] H. Kleykamp, J.O. Paschoal, R. Pejsa, F. Thümmler, Composition and structure of fission product precipitates in irradiated oxide fuels: correlation with phase studies in the Mo-Ru-Rh-Pd and BaO-UO_2-ZrO_2-MoO_2 systems, J. Nucl. Mater. 130 (1985) 426–433, https://doi.org/10.1016/0022-3115(85)90329-0.

[17] H. Kleykamp, The chemical state of the fission products in oxide fuels, J. Nucl. Mater. 131 (1985) 221–246, https://doi.org/10.1016/0022-3115(85)90460-x.

[18] S.C. Middleburgh, D.M. King, G.R. Lumpkin, Atomic scale modelling of hexagonal structured metallic fission product alloys, R. Soc. Open Sci. 2 (2015), 140292. https://doi.org/10.1098/rsos.140292.

[19] M. Peters, J. Hemptenmacher, J. Kumpfert, C. Leyens, Structure and properties of titanium and titanium alloys, in: C.L.a.M. Peters (Ed.), Titanium and Titanium Alloys, Wiley-VCH Verlag GmbH & Co. KGaA, Weinheim 2005, pp. 1–36.

[20] L.-F. Huang, B. Grabowski, J. Zhang, M.-J. Lai, C.C. Tasan, S. Sandlöbes, D. Raabe, J. Neugebauer, From electronic structure to phase diagrams: a bottom-up approach to understand the stability of titanium–transition metal alloys, Acta Mater. 113 (2016) 311–319, https://doi.org/10.1016/j.actamat.2016.04.059.

[21] S.F. Kovtun, R.A. Ul'yanov, Effect of alloying on the physicochemical properties of titanium, in: I.I. Kornilov (Ed.), Physical Metallurgy of Titanium, Science Publishing House, Moscow 1964, pp. 120–136.

[22] J.C. Williams, B.S. Hickman, H.L. Marcus, The effect of omega phase on the mechanical properties of titanium alloys, Metall. Trans. 2 (1971) 1913–1919, https://doi.org/10.1007/BF02913423.

[23] F. Sun, J.Y. Zhang, P. Vermaut, D. Choudhuri, T. Alam, S.A. Mantri, P. Svec, T. Gloriant, P.J. Jacques, R. Banerjee, F. Prima, Strengthening strategy for a ductile metastable β-titanium alloy using low-temperature aging, Mater. Res. Lett. 5 (2017) 547–553, https://doi.org/10.1080/21663831.2017.1350211.

[24] H. Liu, M. Niinomi, M. Nakai, J. Hieda, K. Cho, Changeable Young's modulus with large elongation-to-failure in β-type titanium alloys for spinal fixation applications, Scr. Mater. 82 (2014) 29–32, https://doi.org/10.1016/j.scriptamat.2014.03.014.

[25] H. Liu, M. Niinomi, M. Nakai, K. Cho, β-Type titanium alloys for spinal fixation surgery with high Young's modulus variability and good mechanical properties, Acta Biomater. 24 (2015) 361–369, https://doi.org/10.1016/j.actbio.2015.06.022.

[26] M.J. Lai, T. Li, D. Raabe, ω phase acts as a switch between dislocation channeling and joint twinning- and transformation-induced plasticity in a metastable β titanium alloy, Acta Mater. 151 (2018) 67–77, https://doi.org/10.1016/j.actamat.2018.03.053.

[27] L. Vitos, H.L. Skriver, B. Johansson, J. Kollár, Application of the exact muffin-tin orbitals theory: the spherical cell approximation, Comput. Mater. Sci. 18 (2000) 24–38, https://doi.org/10.1016/S0927-0256(99)00098-1.

[28] L. Vitos, Total-energy method based on the exact muffin-tin orbitals theory, Phys. Rev. B 64 (2001), 014107. https://doi.org/10.1103/PhysRevB.64.014107.

[29] A.V. Ruban, H.L. Skriver, Screened Coulomb interactions in metallic alloys. I. Universal screening in the atomic-sphere approximation, Phys. Rev. B 66 (2002), 024201. https://doi.org/10.1103/PhysRevB.66.024201.

[30] A.V. Ruban, S.I. Simak, P.A. Korzhavyi, H.L. Skriver, Screened Coulomb interactions in metallic alloys. II. Screening beyond the single-site and atomic-sphere approximations, Phys. Rev. B 66 (2002), 024202. https://doi.org/10.1103/PhysRevB.66.024202.

[31] L. Vitos, Computational Quantum Mechanics for Materials Engineers: The EMTO Method and Applications, Springer-Verlag London, London, 2007.

[32] L. Vitos, J. Kollár, H.L. Skriver, Full charge-density calculation of the surface energy of metals, Phys. Rev. B 49 (1994) 16694–16701, https://doi.org/10.1103/PhysRevB.49.16694.

[33] L. Vitos, J. Kollár, H.L. Skriver, Full charge-density scheme with a kinetic-energy correction: application to ground-state properties of the 4d metals, Phys. Rev. B 55 (1997) 13521–13527, https://doi.org/10.1103/PhysRevB.55.13521.

[34] P. Soven, Coherent-potential model of substitutional disordered alloys, Phys. Rev. 156 (1967) 809–813, https://doi.org/10.1103/PhysRev.156.809.

[35] B.L. Gyorffy, Coherent-potential approximation for a nonoverlapping-muffin-tin-potential model of random substitutional alloys, Phys. Rev. B 5 (1972) 2382–2384, https://doi.org/10.1103/PhysRevB.5.2382.

[36] L. Vitos, I.A. Abrikosov, B. Johansson, Anisotropic lattice distortions in random alloys from first-principles theory, Phys. Rev. Lett. 87 (2001), 156401. https://doi.org/10.1103/PhysRevLett.87.156401.

[37] J.P. Perdew, K. Burke, M. Ernzerhof, Generalized gradient approximation made simple, Phys. Rev. Lett. 77 (1996) 3865–3868, https://doi.org/10.1103/PhysRevLett.77.3865.

[38] P. Vinet, J.H. Rose, J. Ferrante, J.R. Smith, Universal features of the equation of state of solids, J. Phys. Condens. Matter 1 (1989) 1941–1963, https://doi.org/10.1088/0953-8984/1/11/002.

[39] A.O.-d. la-Roza, V. Luaña, Gibbs 2: a new version of the quasi-harmonic model code. I. Robust treatment of the static data, Comput. Phys. Commun. 182 (2011) 1708–1720, https://doi.org/10.1016/j.cpc.2011.04.016.

[40] O.N. Senkov, J.M. Scott, S.V. Senkova, F. Meisenkothen, D.B. Miracle, C.F. Woodward, Microstructure and elevated temperature properties of a refractory TaNbHfZrTi alloy, J. Mater. Sci. 47 (2012) 4062–4074, https://doi.org/10.1007/s10853-012-6260-2.

[41] F. Körmann, M.H.F. Sluiter, Interplay between lattice distortions, vibrations and phase stability in NbMoTaW high entropy alloys, Entropy 18 (2016) 403, https://doi.org/10.3390/e18080403.

[42] H. Song, F. Tian, Q.-M. Hu, L. Vitos, Y. Wang, J. Shen, N. Chen, Local lattice distortion in high-entropy alloys, Phys. Rev. Mater. 1 (2017), 023404. https://doi.org/10.1103/PhysRevMaterials.1.023404.

[43] Y. Ikeda, B. Grabowski, F. Körmann, *Ab initio* phase stabilities and mechanical properties of multicomponent alloys: a comprehensive review for high entropy alloys and compositionally complex alloys, Mater. Charact. 147 (2019) 464–511, https://doi.org/10.1016/j.matchar.2018.06.019.

[44] T. Kostiuchenko, F. Körmann, J. Neugebauer, A. Shapeev, Impact of lattice relaxations on phase transitions in a high-entropy alloy studied by machine-learning potentials, npj Comput. Mater. 5 (2019) 55, https://doi.org/10.1038/s41524-019-0195-y.

[45] D. Ma, B. Grabowski, F. Körmann, J. Neugebauer, D. Raabe, *Ab initio* thermodynamics of the CoCrFeMnNi high entropy alloy: importance of entropy contributions beyond the configurational one, Acta Mater. 100 (2015) 90–97, https://doi.org/10.1016/j.actamat.2015.08.050.

[46] Z. Li, F. Körmann, B. Grabowski, J. Neugebauer, D. Raabe, *Ab initio* assisted design of quinary dual-phase high-entropy alloys with transformation-induced plasticity, Acta Mater. 136 (2017) 262–270, https://doi.org/10.1016/j.actamat.2017.07.023.

[47] S. Zhao, G.M. Stocks, Y. Zhang, Stacking fault energies of face-centered cubic concentrated solid solution alloys, Acta Mater. 134 (2017) 334–345, https://doi.org/10.1016/j.actamat.2017.05.001.

[48] C. Niu, C.R. LaRosa, J. Miao, M.J. Mills, M. Ghazisaeidi, Magnetically-driven phase transformation strengthening in high entropy alloys, Nat. Commun. 9 (2018) 1363, https://doi.org/10.1038/s41467-018-03846-0.

[49] Y. Wang, M. Yan, Q. Zhu, W.Y. Wang, Y. Wu, X. Hui, R. Otis, S.-L. Shang, Z.-K. Liu, L.-Q. Chen, Computation of entropies and phase equilibria in refractory V-Nb-Mo-Ta-W high-entropy alloys, Acta Mater. 143 (2018) 88–101, https://doi.org/10.1016/j.actamat.2017.10.017.

[50] B. Grabowski, Y. Ikeda, P. Srinivasan, F. Körmann, C. Freysoldt, A.I. Duff, A. Shapeev, J. Neugebauer, Ab initio vibrational free energies including anharmonicity for multicomponent alloys, npj Comput. Mater. 5 (2019) 80, https://doi.org/10.1038/s41524-019-0218-8.

[51] R.J. Talling, R.J. Dashwood, M. Jackson, D. Dye, On the mechanism of superelasticity in Gum metal, Acta Mater. 57 (2009) 1188–1198, https://doi.org/10.1016/j.actamat.2008.11.013.

[52] Y.L. Hao, S.J. Li, S.Y. Sun, C.Y. Zheng, R. Yang, Elastic deformation behaviour of Ti–24Nb–4Zr–7.9Sn for biomedical applications, Acta Biomater. 3 (2007) 277–286, https://doi.org/10.1016/j.actbio.2006.11.002.

[53] D.B. Williams, C.B. Carter, Transmission Electron Microscopy, 2009.

[54] Y. Zheng, R.E.A. Williams, H.L. Fraser, Characterization of a previously unidentified ordered orthorhombic metastable phase in Ti-5Al-5Mo-5V-3Cr, Scr. Mater. 113 (2016) 202–205, https://doi.org/10.1016/j.scriptamat.2015.10.037.

[55] V. Soni, B. Gwalani, O.N. Senkov, B. Viswanathan, T. Alam, D.B. Miracle, R. Banerjee, Phase stability as a function of temperature in a refractory high-entropy alloy, J. Mater. Res. 33 (2018) 3235–3246, https://doi.org/10.1557/jmr.2018.223.

[56] W.P. Huhn, Thermodynamics From First Principles: Prediction of Phase Diagrams and Materials Properties Using Density Functional Theory, Carnegie Mellon University, 2014.

[57] W.P. Huhn, M. Widom, Prediction of A2 to B2 phase transition in the high-entropy alloy Mo-Nb-Ta-W, JOM 65 (2013) 1772–1779, https://doi.org/10.1007/s11837-013-0772-3.

[58] D.M. King, S.C. Middleburgh, L. Edwards, G.R. Lumpkin, M. Cortie, Predicting the crystal structure and phase transitions in high-entropy alloys, JOM 67 (2015) 2375–2380, https://doi.org/10.1007/s11837-015-1495-4.

[59] P. Singh, A.V. Smirnov, D.D. Johnson, Atomic short-range order and incipient long-range order in high-entropy alloys, Phys. Rev. B 91 (2015), 224204. https://doi.org/10.1103/PhysRevB.91.224204.

[60] F. Körmann, A.V. Ruban, M.H.F. Sluiter, Long-ranged interactions in bcc NbMoTaW high-entropy alloys, Mater. Res. Lett. 5 (2017) 35–40, https://doi.org/10.1080/21663831.2016.1198837.

[61] M. Ogura, T. Fukushima, R. Zeller, P.H. Dederichs, Structure of the high-entropy alloy Al_x CrFeCoNi: fcc versus bcc, J. Alloys Compd. 715 (2017) 454–459, https://doi.org/10.1016/j.jallcom.2017.04.318.

[62] R. Feng, M.C. Gao, C. Zhang, W. Guo, J.D. Poplawsky, F. Zhang, J.A. Hawk, J.C. Neuefeind, Y. Ren, P.K. Liaw, Phase stability and transformation in a light-weight high-entropy alloy, Acta Mater. 146 (2018) 280–293, https://doi.org/10.1016/j.actamat.2017.12.061.

[63] C.G. Schön, T. Duong, Y. Wang, R. Arróyave, Probing the entropy hypothesis in highly concentrated alloys, Acta Mater. 148 (2018) 263–279, https://doi.org/10.1016/j.actamat.2018.01.028.

[64] P. Singh, A.V. Smirnov, D.D. Johnson, Ta-Nb-Mo-W refractory high-entropy alloys: anomalous ordering behavior and its intriguing electronic origin, Phys. Rev. Mater. 2 (2018), 055004. https://doi.org/10.1103/PhysRevMaterials.2.055004.

[65] S. Lee, C. Park, J. Hong, J.T. Yeom, The role of nano-domains in {1011} twinned martensite in metastable titanium alloys, Sci. Rep. 8 (2018) 11914, https://doi.org/10.1038/s41598-018-30059-8.

[66] Y. Linden, M. Pinkas, A. Munitz, L. Meshi, Long-period antiphase domains and short-range order in a B2 matrix of the AlCoCrFeNi high-entropy alloy, Scr. Mater. 139 (2017) 49–52, https://doi.org/10.1016/j.scriptamat.2017.06.015.

[67] E.L. Pang, E.J. Pickering, S.I. Baik, D.N. Seidman, N.G. Jones, The effect of zirconium on the omega phase in Ti-24Nb-[0–8]Zr (at.%) alloys, Acta Mater. 153 (2018) 62–70, https://doi.org/10.1016/j.actamat.2018.04.016.

[68] D. Choudhuri, Y. Zheng, T. Alam, R. Shi, M. Hendrickson, S. Banerjee, Y. Wang, S.G. Srinivasan, H. Fraser, R. Banerjee, Coupled experimental and computational investigation of omega phase evolution in a high misfit titanium-vanadium alloy, Acta Mater. 130 (2017) 215–228, https://doi.org/10.1016/j.actamat.2017.03.047.

[69] F. Sun, J.Y. Zhang, M. Marteleur, T. Gloriant, P. Vermaut, P. Castany, C. Curfs, P.J. Jacques, F. Prima, Deformation microstructure and mechanisms in a metastable β titanium alloy exhibiting TWIP and TRIP effects, Mater. Sci. Forum 783–786 (2014) 1360–1365, https://doi.org/10.4028/www.scientific.net/MSF.783-786.1360.

[70] N.G. Jones, R.J. Dashwood, M. Jackson, D. Dye, β Phase decomposition in Ti–5Al–5Mo–5V–3Cr, Acta Mater. 57 (2009) 3830–3839, https://doi.org/10.1016/j.actamat.2009.04.031.

[71] B.S. Hickman, The formation of omega phase in titanium and zirconium alloys: a review, J. Mater. Sci. 4 (1969) 554–563, https://doi.org/10.1007/bf00550217.

[72] S. Banerjee, R. Tewari, G.K. Dey, Omega phase transformation — morphologies and mechanisms, Int. J. Mater. Res. 97 (2006) 963–977, https://doi.org/10.3139/146.101327.

[73] A. Devaraj, S. Nag, R. Srinivasan, R.E.A. Williams, S. Banerjee, R. Banerjee, H.L. Fraser, Experimental evidence of concurrent compositional and structural instabilities leading to ω precipitation in titanium–molybdenum alloys, Acta Mater. 60 (2012) 596–609, https://doi.org/10.1016/j.actamat.2011.10.008.

[74] A. Devaraj, R.E.A. Williams, S. Nag, R. Srinivasan, H.L. Fraser, R. Banerjee, Three-dimensional morphology and composition of omega precipitates in a binary

titanium–molybdenum alloy, Scr. Mater. 61 (2009) 701–704, https://doi.org/10.1016/j.scriptamat.2009.06.006.
[75] S. Nag, A. Devaraj, R. Srinivasan, R.E.A. Williams, N. Gupta, G.B. Viswanathan, J.S. Tiley, S. Banerjee, S.G. Srinivasan, H.L. Fraser, R. Banerjee, Novel mixed-mode phase transition involving a composition-dependent displacive component, Phys. Rev. Lett. 106 (2011), 245701. https://doi.org/10.1103/PhysRevLett.106.245701.
[76] ASM Aerospace Specification Metals Inc., Titanium Ti-6Al-4V (Grade 5), annealed, http://asmmatweb.com/search/SpecificMaterial.asp?bassnum=MTP641.
[77] AZO materials, titanium alloys — Ti8Al1Mo1V, https://www.azom.com/properties.aspx?ArticleID=1642.